Journal of Materials Science & Technology 141 (2023) 236–244

Contents lists available at ScienceDirect

Journal of Materials Science & Technology

journal homepage: www.elsevier.com/locate/jmst

Research Article

Efficient predictions of formation energies and convex hulls from density functional tight binding calculations

Anshuman Kumar[a], Zulfikhar A. Ali[b], Bryan M. Wong[c,*]

[a] Materials Science & Engineering Program, University of California-Riverside, Riverside, 92521, CA, USA
[b] Department of Physics & Astronomy, University of California-Riverside, Riverside, 92521, CA,USA
[c] Materials Science & Engineering Program, Department of Chemical & Environmental Engineering, Department of Physics & Astronomy, and Department of Chemistry, University of California-Riverside, Riverside,92521, CA,USA

ARTICLE INFO

Article history:
Received 1 August 2022
Revised 14 September 2022
Accepted 25 October 2022
Available online 1 November 2022

Keywords:
CASM
DFTB
DFT
Formation energy
Convex hull

ABSTRACT

Defects in materials significantly alter their electronic and structural properties, which affect the performance of electronic devices, structural alloys, and functional materials. However, calculating all the possible defects in complex materials with conventional Density Functional Theory (DFT) can be computationally prohibitive. To enhance the efficiency of these calculations, we interfaced Density Functional Tight Binding (DFTB) with the Clusters Approach to Statistical Mechanics (CASM) software package for the first time. Using SiC and ZnO as representative examples, we show that DFTB gives accurate results and can be used as an efficient computational approach for calculating and pre-screening formation energies/convex hulls. Our DFTB+CASM implementation allows for an efficient exploration (up to an order of magnitude faster than DFT) of formation energies and convex hulls, which researchers can use to probe other complex systems.

1. Introduction

Point defects, such as vacancies, play a vital role in the electronic and structural properties of semiconductor materials. These properties ultimately dictate the performance of electronic devices, structural alloys, and functional materials; therefore, a deep understanding of vacancies at the atomistic level can provide a rational path toward their improvement [1–4]. One of the most important quantities to characterize a defect is its formation energy, which can, in principle, be computed with Density Functional Theory (DFT) [5,6]. Although accurate and widely transferable, DFT can be computationally prohibitive for the routine exploration of the numerous types of defects in material systems. Alternatively, semi-empirical methods, such as Density Functional Tight Binding (DFTB) [7–10], have recently emerged as efficient approaches for addressing these computational bottlenecks. In particular, the DFTB formalism has already been used to calculate a variety of large systems such as metallic nanoparticles [11,12], explicitly-solvated chromophores [13], massive biological structures [14], molecules/clusters with numerous conformations [15,16], and immense nanostructures [17].

To enable fast and accurate calculations of formation energies, we combined DFTB with the Clusters Approach to Statistical Mechanics (CASM) [18,19] software package to predict thermodynamically stable phases of materials for the first time. Specifically, our new capability allows the rapid and accurate calculation of formation energies and the convex hull (if favorable). In short, the convex hull provides a global view of the relative stabilities of structures after the formation energies are calculated. Although computationally demanding, the calculation of formation energies and convex hulls has enabled the discovery of new materials, including superconducting hydrides [20–24], metal nitrides [25], and metal carbides [26]. Predicting the convex hull for general materials is time-consuming since it requires the classification of a vast number of energy minima on the lattice energy surface. Software programs, such as USPEX [27,28] and CALYPSO [29,30] have been used to explore the vast compositional phase space of these materials. Compared to other crystal structure prediction codes, the main advantage of CASM is its ability to evaluate the kinetic and ther-

* Corresponding author.
E-mail address: bryan.wong@ucr.edu (B.M. Wong).
URL: http://www.bmwong-group.com (B.M. Wong)

https://doi.org/10.1016/j.jmst.2022.10.002

modynamic properties of multi-component crystalline solids using group theoretical techniques.

Using this new capability, we calculate the formation energies of various silicon carbide (SiC) and zinc oxide (ZnO) configurations to highlight the efficiency of our DFTB+CASM implementation. SiC is one of the most promising materials for high-temperature, radiation-resistant, power and high-speed electronics [31–34]. ZnO is an affordable, earth-abundant, wide-band-gap transparent conducting oxide with applications in electronics, optoelectronics, pharmaceuticals, sensors, and catalysis [35]. ZnO crystallizes in many forms, with hexagonal wurtzite (B4), zinc blende (B3), and cubic rocksalt (B1) being the most common. Using SiC and ZnO as representative examples, we compare the accuracy and efficiency of DFTB and DFT for predicting formation energies and convex hulls of these binary compounds.

Our paper is organized as follows: Section 2 gives a brief overview of DFTB, DFT, structure generation algorithm in CASM, formation energies, and convex hulls. Section 3 provides computational details, and Section 4 presents our results and discussion. Finally, we conclude with closing remarks and a summary in Section 5.

2. Theory and methodology

2.1. DFTB

Before proceeding with a discussion of our approach for evaluating the formation energy/convex hull, we briefly review the DFTB formalism. DFTB is based on a Taylor series expansion of the DFT Kohn-Sham (KS) total energy, E_{KS}, with respect to electron density fluctuations $\rho(r) = \rho_0(r) + \delta\rho(r)$, where $\rho_0(r)$ is a reference density of neutral atomic species. In our work, we use the second-order expansion of the KS energy, abbreviated as DFTB2 [36]. The unmodified KS total energy is given by

$$E_{\mathrm{KS}} = \sum_{i}^{\mathrm{occ}} \langle\psi_i| -\frac{1}{2}\nabla^2 + V_{\mathrm{ext}} |\psi_i\rangle + E_{\mathrm{H}} + E_{\mathrm{xc}} + E_{\mathrm{II}}, \tag{1}$$

where ψ_i are the KS orbitals, V_{ext} is the external potential, E_{H} is the Hartree energy, E_{XC} is the exchange-correlation (XC) energy, and E_{II} is the ion-ion interaction energy. Rewriting Eq. (1) in terms of $\rho(r)$ and expanding up to second order, we obtain the DFTB energy:

$$\begin{aligned} E_{\mathrm{DFTB}} &= \textstyle\sum_i^{\mathrm{occ}} \langle\psi_i| \hat{H}_0 |\psi_i\rangle + \frac{1}{2}\sum_{\mathrm{AB}}^{\mathrm{M}} \gamma_{\mathrm{AB}}\Delta q_{\mathrm{A}}\Delta q_{\mathrm{B}} + E_{\mathrm{rep}}^{\mathrm{AB}} \\ &= E_{\mathrm{BS}} + E_{\gamma} + E_{\mathrm{rep}}, \end{aligned} \tag{2}$$

where the second term sums over the number of atoms, M, in the system.

The first term in Eq. (2), E_{BS}, corresponds to the band structure energy (i.e., the sum over the occupied orbital energies) obtained from the diagonalization of the non-self-consistent DFTB Hamiltonian, $\hat{H_0}$:

$$\hat{H_0} = \langle\phi_\mu| \hat{T} + v_{\mathrm{eff}}[\rho_0^{\mathrm{A}} + \rho_0^{\mathrm{B}}] |\phi_\nu\rangle, \quad \mu \in \mathrm{A},\ \nu \in \mathrm{B}, \tag{3}$$

where ϕ_μ, ϕ_ν forms a minimal Slater type atomic basis (μ and ν are the indices of the valence atomic basis function centered on atoms A and B, respectively), $\hat{T}$ is the kinetic energy operator, ρ_0^{I} is the reference density of neutral atom I, and v_{eff} is an effective Kohn-Sham potential. As shown in Eq. (3), only two-center elements are treated within the DFTB framework, which are explicitly calculated using analytical functions within the linear combination of atomic orbitals (LCAO) formalism. The Hamiltonian and overlap matrix elements are pre-computed and stored in Slater-Koster (SK) files for all pairs of chemical elements as a function of the distance between atomic pairs. Thus, no explicit integral evaluation occurs during the simulation, which significantly improves the computational efficiency of the DFTB approach. The second term in Eq. (2), E_γ, is the energy due to charge fluctuations, where γ_{AB} is an analytical function of the interatomic distance, and the Hubbard parameter U takes into account the electron-electron interaction. The Hubbard parameter U is related to the hardness of the atoms and controls how the electron density is distributed between the atoms. The $\Delta q_{\mathrm{A/B}}$ term ($= q_{\mathrm{A/B}} - q^0_{\mathrm{A/B}}$) is the net charge of atom A/B. The summation in the E_γ term in Eq. (2) is performed over the number of atoms, M, in the system. The last term, E_{rep}, is the distance-dependent diatomic repulsive potential, which includes core-electron effects, ion-ion repulsion, and a portion of exchange-correlation effects. The pairwise repulsive functions are obtained by fitting to DFT calculations using a suitable reference structure and, like the matrix elements, are pre-tabulated. By applying the variational principle, we obtain the DFTB Kohn-Sham equations:

$$\sum_{\mathrm{B}}\sum_{\nu\in\mathrm{B}}^{\mathrm{M}} c_{\nu i}\left(H_{\mu\nu} - \epsilon_i S_{\mu\nu}\right) = 0, \quad \forall \mathrm{A}, \mu \in \mathrm{A}, i, \tag{4}$$

where the DFTB Hamiltonian is given by

$$H_{\mu\nu} = \langle\phi_\mu| \hat{H}_0 |\phi_\nu\rangle + S_{\mu\nu}\textstyle\sum_\xi^{\mathrm{M}} \Delta q_\xi \left(\frac{1}{2}\left(\gamma_{\mathrm{A}\xi} + \gamma_{\mathrm{B}\xi}\right)\right), \tag{5}$$

with $\mu \in \mathrm{A}$, $\nu \in \mathrm{B}$, and $S_{\mu\nu}$ is the overlap matrix of the atomic orbitals. Because the atomic charges are dependent on the one-particle wave functions, ψ_i, Eq. (5) must be solved iteratively until self-consistency is reached.

DFTB is a tight-binding-based method and provides a reasonable accuracy at a much lower computational cost compared to DFT calculations. As mentioned earlier, the Hamiltonian and the overlap matrix elements $H_{\mu\nu}$ and $S_{\mu\nu}$ are pre-computed and tabulated; i.e., they are not computed during the execution of the program. This and the use of a minimal valence basis set can typically lead to huge computational savings (2–3 orders of magnitude) compared to full DFT.

2.2. DFT

In Kohn-Sham DFT (KS-DFT), the electronic energy of a system is given by

$$E[\rho] = T_{\mathrm{KS}}[\rho] + E_{\mathrm{ext}}[\rho] + E_{\mathrm{H}}[\rho] + E_{\mathrm{xc}}[\rho]. \tag{6}$$

All of the terms in Eq. (6) are a functional of the density ρ, where $T_{\mathrm{KS}}[\rho]$ is the kinetic energy of the electrons, $E_{\mathrm{ext}}[\rho]$ is the attractive interaction between the electrons and the nuclei (also known as the external potential energy), $E_{\mathrm{H}}[\rho]$ is the classical (Coulomb) electrostatic energy of the electronic density charge distribution (also known as the Hartree energy), and $E_{\mathrm{xc}}[\rho]$ is the exchange-correlation energy which describes exchange and correlation quantum interactions.

DFT calculations are performed in an iterative way, with the electron density, $\rho(\vec{r})$, expressed as the sum of one-electron wave functions, ψ_i, known as molecular orbitals (MOs):

$$\rho\left(\vec{r}\right) = \sum_{i=1}^{\mathrm{N_e}} \left|\psi_i\left(\vec{r}\right)\right|^2. \tag{7}$$

These MOs are obtained by solving the Kohn-Sham (KS) eigenvalue equation:

$$\left[-\frac{1}{2}\nabla^2 + V_{\mathrm{ext}}(\boldsymbol{r}) + V_{\mathrm{H}}[\rho](\boldsymbol{r}) + V_{\mathrm{xc}}[\rho](\boldsymbol{r})\right]\psi_i(\boldsymbol{r}) = \epsilon_i\psi_i(\boldsymbol{r}), \tag{8}$$

where $V_{\mathrm{H}}[\rho]$ and $V_{\mathrm{xc}}[\rho]$ are themselves functionals of the density (making them functionals of the MOs), which are obtained after solving the KS eigenvalue problem in Eq. (8). As such, the KS eigenvalue problem in Eq. (8) cannot be solved directly and must be calculated in an iterative fashion within a self-consistent field

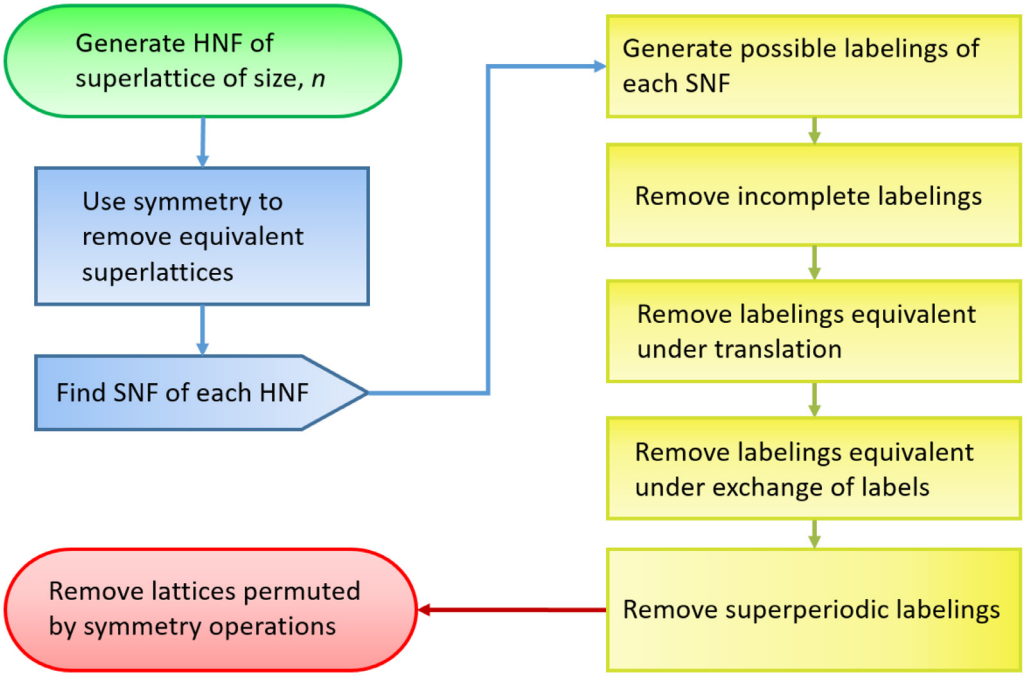

Fig. 1. Flowchart of the structure generation algorithm used in the CASM software package to enumerate structures.

(SCF) method. In this iterative process, a set of guess wavefunctions, $\{\psi_i\}$, are used to compute the terms in Eq. (8). This then allows the calculation of a new set of $\{\psi_i\}$, and the process repeats until $\{\psi_i\}$ and the energy in Eq. (6) are converged.

One of the key computational bottlenecks in KS-DFT is the numerous three-dimensional integrals that are evaluated in each SCF step, which is extremely time-consuming. Since DFTB uses precomputed integrals in each SCF cycle, its performance can be significantly faster (up to 2–3 orders of magnitude) than full DFT calculations.

2.3. Structure generation with CASM

The algorithms in the CASM software package that enumerate symmetrically distinct configurations utilize an approach based on Hermite Normal Forms of integer matrices [37,38]. The following is a brief outline of the algorithm [39], shown schemataically in Fig. 1:

(1) All Hermite normal form (HNF) matrices are generated for each superlattice of size n.
(2) The symmetry of the parent lattice is used to remove rotationally equivalent superlattices, thus shrinking the list of HNF matrices.
(3) For each index n of the superlattice, the Smith normal form (SNF) is determined for each HNF in the list.
  (a) A list of possible labelings (atomic configurations) is generated for each SNF, which is a list of all k^n numbers in a base k, n-digit system. For the labels, the first k letters of the alphabet, (a, b, $\cdots$) are used.
  (b) Incomplete labelings, where each of the k labels (a, b, $\cdots$) does not appear at least once, are removed.
  (c) Labelings that are equivalent under the translation of the parent lattice vectors are removed. This reduces the list labelings by a factor of $\sim n$.
  (d) Labelings that are equivalent under an exchange of labels, i.e., $a \rightleftharpoons b$, are removed (for example, the labeling *aabbaa* is removed from the list because it is equivalent to *bbaabb*).
  (e) Superperiodic labelings that correspond to a non-primitive superstructure are removed. This can be done without using the geometry of the superlattice.
(4) Labelings are removed for each HNF that are permuted by symmetry operations (of the parent lattice) that leave the superlattice fixed.

An important feature of this algorithm is that the list of possible labelings, generated in step (3)-(a), forms a minimal hash table with a perfect hash function. All duplicate labelings in a list of N can be eliminated and accomplished in $O(N)$ time. Coupled with the group-theoretical approaches in CASM, this results in a highly efficient algorithm that is orders of magnitude faster than the algorithm of Ferreira, Wei, and Zunger [40].

2.4. Formation energy

The formation energy, e^{f}, is normalized per primitive unit cell of a particular atomic configuration, σ. For a binary compound AB_x (in this work, atom A is Si/Zn, and atom B is C/O), the formation energy can be calculated with the expression:

$$e^{\mathrm{f}}(\sigma) = e(\sigma) - e^{\mathrm{ref}}(x), \tag{9}$$

where $e^{\mathrm{f}}(\sigma)$ is the formation energy of configuration σ, $e(\sigma)$ is the DFT/DFTB total energy (normalized per primitive unit cell) of configuration σ, and $e^{\mathrm{ref}}(x)$ is the DFT/DFTB total energies (normalized per primitive unit cell) of reference state with composition x. The energy of the reference state, $e^{\mathrm{ref}}(x)$, is calculated from the following expression:

$$e^{\mathrm{ref}}(x) = e^{\mathrm{ref}}(x_1) + (x - x_1)\frac{e^{\mathrm{ref}}(x_2) - e^{\mathrm{ref}}(x_1)}{x_2 - x_1}, \tag{10}$$

where $e^{\mathrm{ref}}(x_1)$ and $e^{\mathrm{ref}}(x_2)$ are the DFT/DFTB calculated total energies (normalized per primitive unit cell) of the reference states with composition x_1 and x_2, respectively. The composition, x, can be calculated from the expression:

$$x = 1 - (\mathrm{B}_n/\mathrm{A}_n), \tag{11}$$

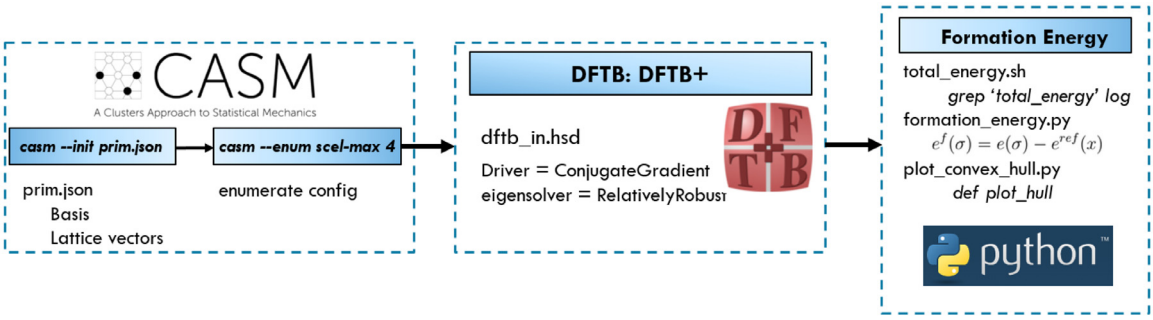

Fig. 2. General workflow in our DFTB+CASM implementation for calculating formation energies and the convex hull.

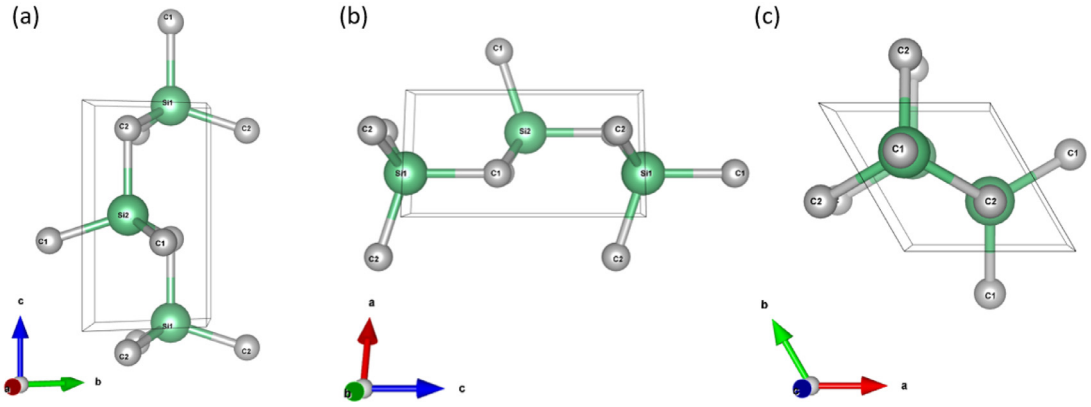

Fig. 3. Primitive unit cells used to generate the various supercells and configurations. Using the CASM software package, we generate all symmetrically distinct configurations with the stoichiometry Si_2C_2. Panels (a), (b), and (c) show the primitive cell in different orientations. Light green and grey atoms represent Si and C, respectively. The reader should refer to the web version of this article regarding any reference to colors used in the figure.

where B_n and A_n denote the number of C (O) and Si (Zn) atoms in the unit cell, respectively. A value of $x = 1$ implies that the unit cell has only Si (Zn) atoms, while $x = 0$ implies that the unit cell consists of an equal number of Si (Zn) and C (O) atoms. In this study, we chose x_1 and x_2 as 0 and 1, respectively. Setting $x_1 = 0$ and $x_2 = 1$ in Eq. (10), the reference state energy, $e^{\text{ref}}(x)$, for a composition x simplifies to:

$$e^{\text{ref}}(x) = e^{\text{ref}}(x_1 = 0) + x\left(e^{\text{ref}}(x_2 = 1) - e^{\text{ref}}(x_1 = 0)\right). \quad (12)$$

Table 1
Initial/experimental lattice parameters of SiC (2H) and ZnO (B4).

Structure	Lattice Vectors (Å)			Lattice Angles		
	a	*b*	*c*	*α*	*β*	*γ*
SiC (2H)	3.076	3.076	5.048	90.00°	90.00°	120.00°
ZnO (B4)	3.302	3.302	5.275	90.00°	90.00°	120.00°

3. Computational details

The general workflow of our calculations is depicted in Fig. 2. We explore thermodynamically stable compositions for binary compounds of the form $A_2B_{2(1-x)}$ using the following four steps: (1) determination of the most stable crystal structure at a fixed composition x using CASM integrated with DFTB, (2) calculation of the formation energy e^f of the compound with respect to its composition at $x = 0$ and $x = 1$, (3) repeating the same calculations by changing x, and (4) plotting the formation energy per fixed composition, e^f vs. x. Details of each step are given below.

3.1. CASM

To generate the configuration space for the various material compositions, we start with the primitive unit cell of 2H-SiC and B4-ZnO (the 2H prefix denotes a two-layer hexagonal symmetry stacking periodicity). The 2H-SiC unit cell is shown in Fig. 3, where the large green atoms represent silicon, and the small gray atoms are carbon. The crystal structure is an AB-type covalent bond crystal, and each Si atom is surrounded by four C atoms. Each 2H-SiC unit cell contains two Si and two C atoms. The space group of 2H-SiC is $P6_3mc$, and the experimental lattice parameters are shown in Table 1. B4-ZnO (Wurtzite) has a similar unit cell as 2H-SiC, but is not shown here for brevity. Table 1 also lists the experimental lattice parameters of the 2H-SiC [41,42] and B4-ZnO [43] unit cells used to generate different configurations. Both 2H-SiC and B4-ZnO follow the AB type stacking sequence. The DFT-optimized SiC lattice parameters are $a = b = 3.084$ Å and $c = 5.065$ Å with $\alpha = \beta = 90^\circ$ and $\gamma = 120^\circ$. DFTB gives similar optimized lattice parameters with $a = b = 3.173$ Å and $c = 5.235$ Å with $\alpha = \beta = 90^\circ$ and $\gamma = 119.99^\circ$. As such, the DFT- and DFTB-optimized lattice parameters match extremely well (within 0.1 Å) with the experimental parameters in Table 1 (Table S1 in the supplementary material gives a similar comparison for ZnO). We consider a binary ordering between two C/O atoms and a vacancy at the C/O lattice sites in the unit cell. All symmetrically distinct supercells and derivative configurations (up to a supercell volume that is 4 times the primitive unit cell) were generated using the algorithm developed by Hart et al. [39,44] in the CASM code. This algorithm enumerates superlattices and atomic configurations in a geometry-independent way using the concept of quotient groups associated with each superlattice to determine all unique atomic configurations. We follow the standard procedure for calculating the formation energy/convex hull [45] using DFT/DFTB with the CASM code.

After defining the basis and lattice vectors of the system, the symmetrically distinct configurations are generated using the CASM software package. All configurations in symmetrically distinct supercells were generated in 2H and B4 symmetries for SiC and ZnO, respectively. The primitive unit cell, as shown in Fig. 3, was used to generate the 401 derivative supercell configurations for each SiC and ZnO system. In the last panel of Fig. 2, we calculate the total energies for each configuration via DFT and DFTB.

3.2. DFT Calculations

Density functional theory calculations were carried out with the Vienna Ab Initio Software Package (VASP) code [46,47]. We used projector augmented wave (PAW) pseudopotentials [48,49], and the generalized gradient approximation (GGA) exchange-correlation functional, as parameterized by Perdew, Burke, and Ernzerhof (PBE) [50]. We calculated the total energies using a plane-wave energy cutoff of 400 and 520 eV for SiC and ZnO, respectively. All of our calculations used the standard VASP pseudopotentials for all of the atoms. We used a Γ-point centered Monkhorst-Pack k-point mesh (approximately 12 × 12 × 6) for both SiC and ZnO, and the total energies were found to be suitably converged with this k-point sampling. The k-point sampling differs depending on the unit cell of each configuration, and the CASM software package keeps the mesh density constant for all configurations [51]. In all the optimizations, the geometry was relaxed such that all the forces were less than 0.04 eV/Å. The energy convergence for the electronic degree of freedom was set to 10^{-5} eV. While performing geometry optimizations, the atomic positions, lattice parameters, and angles were allowed to relax for each structure.

3.3. DFTB Calculations

As discussed earlier, DFTB is an approximate tight-binding scheme with a low computational cost due to the use of parameterized integrals and a minimal valence basis set [36,52–57]. In the present study, we used the self-consistent charge formulation of DFTB (SCC-DFTB) in its second-order scheme (DFTB2), which includes the second-order term in the DFT energy expansion around the reference density [58]. Previous studies have shown DFTB to be particularly well suited for describing both SiC and ZnO materials [59–63]. In all of our SiC DFTB calculations, we used a recent DFTB parameterization that accurately reproduces a large dataset of DFT calculations, which includes potential energy surfaces, energies, and forces [64]. We designate the SiC SK files from Ref. [64] as SKflV throughout this paper. For our ZnO DFTB calculations, we used standard parameters from the znorg-0-1 SK set [65]. We used a similar k-point mesh as mentioned in the DFT calculations section. In all of our DFTB calculations, the geometry was relaxed with periodic boundary conditions such that all the forces were less than 0.04 eV/Å, and the SCC convergence tolerance was set to 10^{-5} a.u. Both the DFT and DFTB calculations were carried out in a spin-unpolarized formalism. After optimizing the structures, the formation energies and convex hull plots were produced using bash and python scripts.

3.4. Formation energy

As depicted in the last panel of Fig. 2, the formation energy for each structure is calculated. The 'total energy.sh' script creates a file that contains the optimized DFT/DFTB ground state energy of each of the configurations. In the next step, the 'formation_energy.py' python script reads the ground-state energies and uses Eqs. (10) and (9) to compute the formation energy of each of the configurations. Finally, the 'plot_convex_hull.py' python script is used to plot the convex hull from the DFT/DFTB computed formation energies. In the case of SiC, we constructed the convex hull by connecting all the minima of the negative formation energies at various compositions, x, with straight lines.

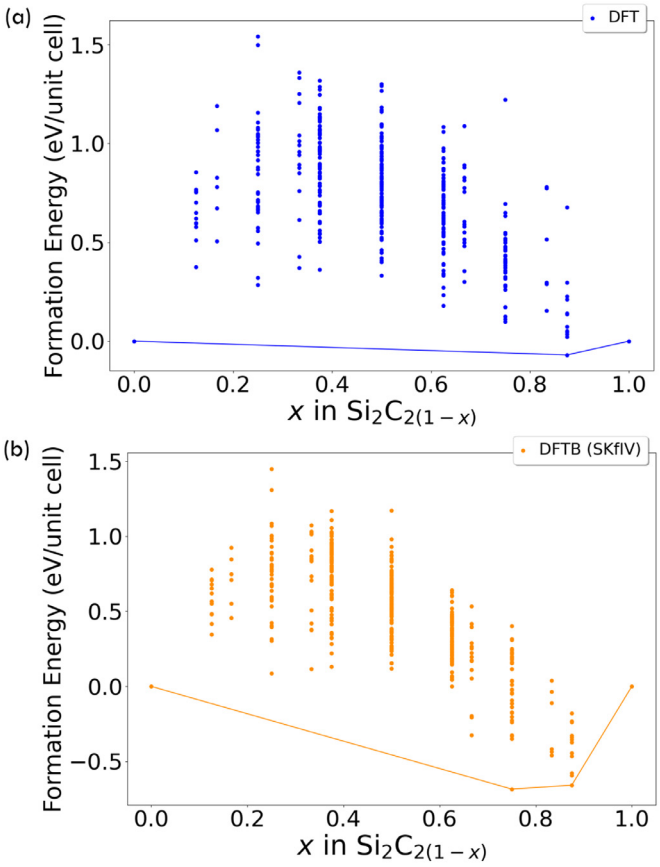

Fig. 4. Formation energy convex hull for the Si-C binary system computed with DFT and DFTB. Panel (a) shows the DFT formation energy. Panel (b) shows the DFTB formation energy calculated using the SKflV SK files. Each point corresponds to a different crystal structure.

4. Results and discussion

Using the configuration space described above, we generated distinct compositions up to 4 times the primitive unit cell volume, which produces a total of 401 symmetrically distinct configurations for SiC and ZnO, each. All the structures used in this work can be downloaded at https://github.com/Anshuman5/data. The DFT and DFTB energies of all the enumerated configurations were calculated to obtain the formation energy using Eq. (9).

4.1. SiC

4.1.1. Convex hull

Fig. 4(a) and (b) show the formation energies of various SiC configurations calculated with DFT and DFTB, respectively. Although the DFT and DFTB calculations find different minima on the convex hull plot, the results match qualitatively. DFTB predicts a minimum at composition $x = 0.75$ while DFT has a minimum nearby at $x = 0.875$. The two minima structures in the DFTB convex hull plot at $x = 0.75$ and $x = 0.875$ have a formation energy difference of 0.025 eV. This small energy difference is due to the approximations in the SK parameters inherent to the DFTB formalism.

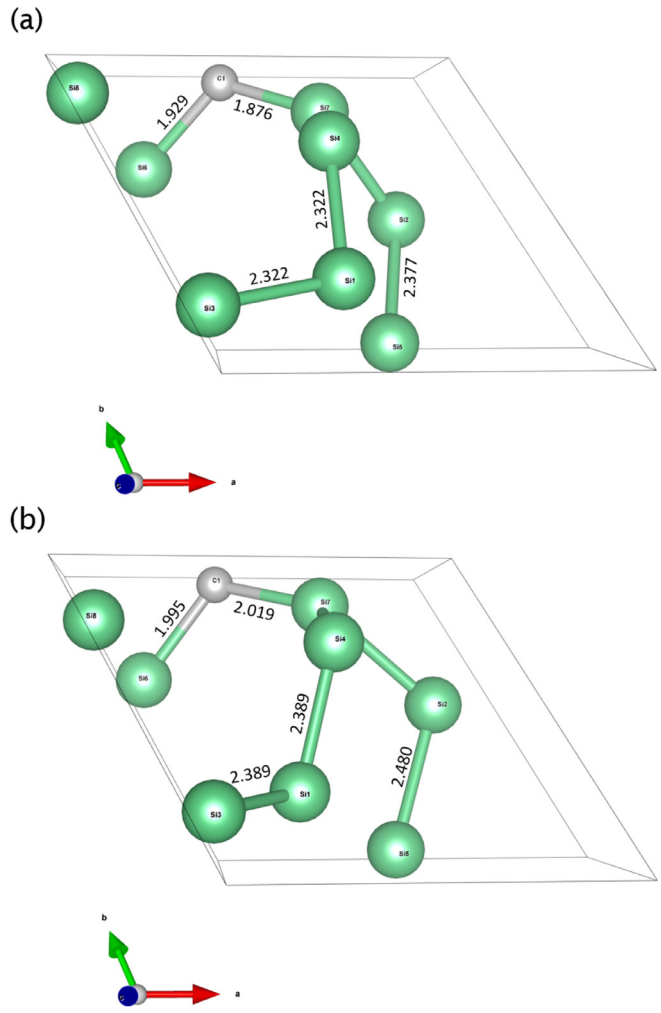

Fig. 5. Comparison of SiC structural parameters (located on the convex hull) after optimization with (a) DFT and (b) DFTB (SKflV), visualized along lattice vector $\vec{c}$. Bond lengths are in Angstroms, and light green and grey atoms represent Si and C, respectively. (The reader should refer to the web version of this article regarding any reference to colors used in the figure.)

The most probable reason for this small discrepancy in the formation energy is the parameterization of the repulsive DFTB potential between the Si and C atoms in the SKflV SK files. The repulsive potentials in the SKflV SK files result in a much stronger repulsion between the Si and C atoms, increasing the bond length between the atoms in the structures, which alters their energetics. A similar phenomenon was also observed in a previous study using TiO_2 DFTB SK files [66]. Nevertheless, our results show that the DFT and DFTB formation energies for SiC are similar; if more accurate results are desired, configurations near the convex hull could be first down-selected via DFTB and subsequently refined/recalculated with DFT to improve their accuracy (which would be more efficient than computing all 401 structures with DFT alone).

4.1.2. Structure comparison

The most stable crystal structure obtained via DFT and DFTB is depicted in Fig. 5. DFTB predicts a minimum at $x = 0.75$ while DFT gives a minimum nearby at $x = 0.875$. The two minima structures in the DFTB convex hull plot at $x = 0.75$ and $x = 0.875$ have a formation energy difference of 0.025 eV. As discussed in the previous section, this discrepancy in the minima for the DFTB formation energy results from approximations in the repulsive potential between the Si and C atoms in the SKflV SK files. Moreover, the crystal structures at $x = 0.875$ obtained via DFT and DFTB show the same P1 symmetry, which consists of eight Si atoms and one C atom in the unit cell (see Fig. 5). Since both the DFT and DFTB calculations correctly predict the same crystal structure and relative ratio of Si/C at $x = 0.875$, our results show that DFTB can be employed as an efficient computational approach tool for calculating and pre-screening formation energies.

Table 2
Comparison of optimized lattice parameters of the minima structure calculated with DFT and DFTB for SiC.

Method	Lattice Vectors (Å)			Lattice Angles		
	a	*b*	*c*	α	β	γ
DFT	6.15	6.15	6.16	121.39°	97.24°	110.62°
DFTB (SKflV)	6.27	6.27	6.40	119.38°	99.60°	109.24°

Fig. 5 compares the DFT and DFTB optimized structural parameters of the most stable configurations at the convex hull minimum located at $x = 0.875$. Two types of Si atoms exist in the unit cell: one that is bonded to only Si atoms and another which is bonded with one C atom. Each Si and C atom has a coordination number of 4. As can be seen in Fig. 5(a), the Si-C bond length ranges from 1.93 to 2.38 Å in the DFT-optimized structure. Fig. 5(b) shows the bond lengths between various Si and C atoms of the DFTB-optimized structure. DFTB predicts slightly longer bond lengths for almost all the Si-C bonds, which on average are longer by 0.06 Å compared to DFT calculations. Table 2 compares the optimized lattice parameters of the minimum structure calculated with DFT and DFTB. DFTB overestimates the optimized lattice parameters and predicts slightly longer lengths for $\vec{a}$, $\vec{b}$, and $\vec{c}$.

As stated earlier, the discrepancy in the structural parameters is due to the parameterization of the repulsive DFTB potential between the Si and C atoms in the SKflV SK files. The repulsive potentials used in the SKflV SK files result in a much stronger repulsion between the Si and C atoms which increases the bond length between the atoms in the structures. Previous work has also shown that DFTB predicts longer lattice parameters for systems containing C atoms [67].

4.2. ZnO

4.2.1. Formation energy

We now proceed to ZnO, which is an even more complex material but shows more accurate results between DFT/DFTB. The wurtzite (B4) structure is the most stable form of ZnO at ambient conditions in nature [68]. The zinc blende (B3) structure of ZnO has a less stable cohesive energy than the B4 structure, and is, therefore, energetically unfavorable at zero temperature and pressure [69]. As such, we enumerated various ZnO configurations starting with the B4-ZnO unit cell. We obtain a significant performance improvement for ZnO structures optimized via DFTB (more details on efficiency are discussed in the next section). It is interesting to note that both the DFT and DFTB calculations do not find a convex hull in the formation energy plots of the $Zn_2O_{2(1-x)}$ binary compounds. As shown in Fig. 6, the calculated formation energies are all positive, showing no stable minima predicted at any composition *x*. A previous study reported similar findings of positive formation energies when oxygen vacancies were introduced in the ZnO lattice [70]. Specifically, these previous studies showed that defects often induce occupied states in the bandgap and increase the formation energy [71–74].

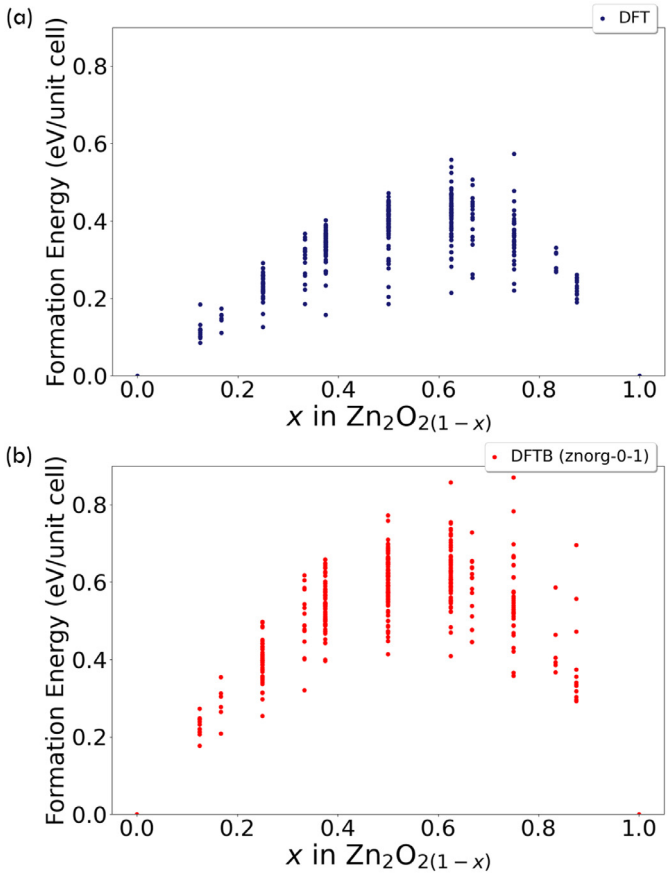

Fig. 6. Formation energy of the ZnO binary system obtained from DFT and DFTB. Panel (a) shows the DFT formation energy, and panel (b) shows the DFTB formation energy calculated using the znorg-0-1 SK files. Each point corresponds to a different crystal structure.

It is interesting to note that the formation of ZnO (Fig. 6) has a larger error than SiC (Fig. 4). This larger error is due to the znorg-0-1 SK files [65] being parameterized from the bandstructure energies, unlike the SiC SK files, which are parameterized from formation energies [64].

4.3. Efficiency analyses for DFT and DFTB

In this section, we give a detailed analysis of the computational timings and efficiency of DFT and DFTB. Fig. 7 compares the wall time per SCF iteration step (WT-SCF) as a function of the number of electrons in various ZnO configurations. As the number of electrons increases, the WT-SCF increases rapidly for both DFT and DFTB. For example, the DFT WT-SCF for a 30-electron ZnO configuration is around 16 s, whereas a 120-electron configuration is roughly 134 s. Fitting the DFT WT-SCF data to a cubic polynomial gives a high R^2 correlation coefficient of 0.92, indicating an $O(N^3)$ scaling, where N is the number of electrons. This scaling can be attributed to matrix diagonalization in KS DFT, which is an $O(N^3)$ process, where N is the size of the matrix. Similarly, fitting the DFTB WT-SCF data gives an $O(N)$ linear scaling with an R^2 of 0.91. For all configurations, the DFTB WT-SCF is less than 6 secs, which is significantly faster than DFT. As can be seen from Fig. 7, the DFTB WT-SCF for a ZnO configuration with 138 electrons is an order of magnitude faster than DFT. It is worth mentioning that although the DFTB WT-SCF is more efficient than DFT, DFTB geometry optimizations may take more SCF cycles compared to DFT, which may result in a small loss in efficiency.

4.3.1. Computational timings for SiC

Fig. 8(a) and (b) compare computational timings for geometry optimizations of various $Si_2C_{2(1-x)}$ structures using DFT (VASP) and DFTB (DFTB+). In general, the DFTB calculations take significantly less time compared to DFT, and Fig. 8(b) shows that DFTB can be an order of magnitude faster than DFT in some cases. For most configurations, the DFTB calculations required more SCF cycles for geometry optimization compared to DFT; however, the total compute time for DFTB is still significantly smaller.

4.3.2. Computational timings for ZnO

Fig. 9 compares wall times for geometry optimization for various $Zn_2O_{2(1-x)}$ binary compounds calculated via DFT and DFTB. As in the case of SiC, Fig. 9(b) shows that DFTB is an order of magnitude faster than DFT in most cases. It is important to note that DFTB is almost 40 times faster than DFT for $Zn_2O_{2(1-x)}$ binary compounds (see Fig. 9(b)), whereas the maximum performance enhancement of DFTB is only 10 times for $Si_2C_{2(1-x)}$. In general, as the number of electrons in the system increases, we show that DFTB exhibits more performance gains than conventional KS DFT calculations.

Finally, Fig. 10 compares the total time (sum of individual wall times) for the geometry optimization of $Si_2C_{2(1-x)}$ and $Zn_2O_{2(1-x)}$ binary compounds. For $Si_2C_{2(1-x)}$, the total time for geometry optimization of all 401 configurations is around five days for DFTB, whereas the DFT calculations require nearly ten days. The difference in performance between DFTB and DFT for $Zn_2O_{2(1-x)}$ is even more significant—DFTB geometry optimizations take approximately 5 days, whereas the DFT calculations take nearly 18 days (more than 3 times longer than DFTB). As mentioned previously, larger systems such as ZnO (which contain more electrons), scale more favorably with DFTB, resulting in speedups that can be orders of magnitude faster than conventional DFT methods.

5. Conclusion

In closing, we have interfaced DFTB with the CASM software package for the first time to enable routine and efficient calculations of formation energies and convex hulls. Our extensive calculations show that DFTB can be used as an efficient screening tool to compute the numerous formation energies (and convex hull if it exists) of complex materials. To highlight the efficiency and accuracy of our approach, we calculated and compared the formation energies of SiC and ZnO with both DFT and DFTB. We find that the DFTB approach enables extremely efficient calculations of formation energies in a completely unbiased manner to predict low-lying metastable phases over the entire composition space. By comparing the convex hull/formation energy from both approaches, we found that DFTB gives similar trends as the DFT calculations. Finally, we performed an extensive benchmark of the computational timings for both DFT and DFTB and found that the DFTB calculations can be an order of magnitude faster (larger systems give even higher computational efficiency). Moreover, we show that DFTB gives accurate results and can be used as an efficient computational approach for calculating and pre-screening formation energies/convex hulls. In summary, our DFTB+CASM implementation allows for an efficient exploration (up to an order of magnitude faster than DFT) of formation energies and convex hulls, which researchers can use to routinely probe other complex systems.

Declaration of Competing Interest

The authors declare that they have no known competing financial interests or personal relationships that could have appeared to influence the work reported in this paper.

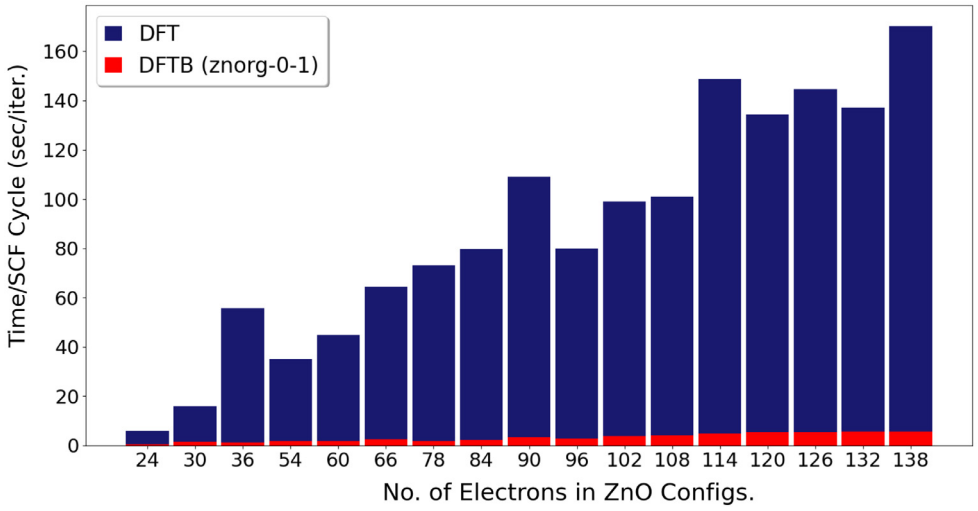

Fig. 7. Comparison of DFT and DFTB wall times per SCF iteration step as a function of the number of electrons in various ZnO configurations. Each vertical bar value was calculated by averaging multiple configurations having the same number of electrons.

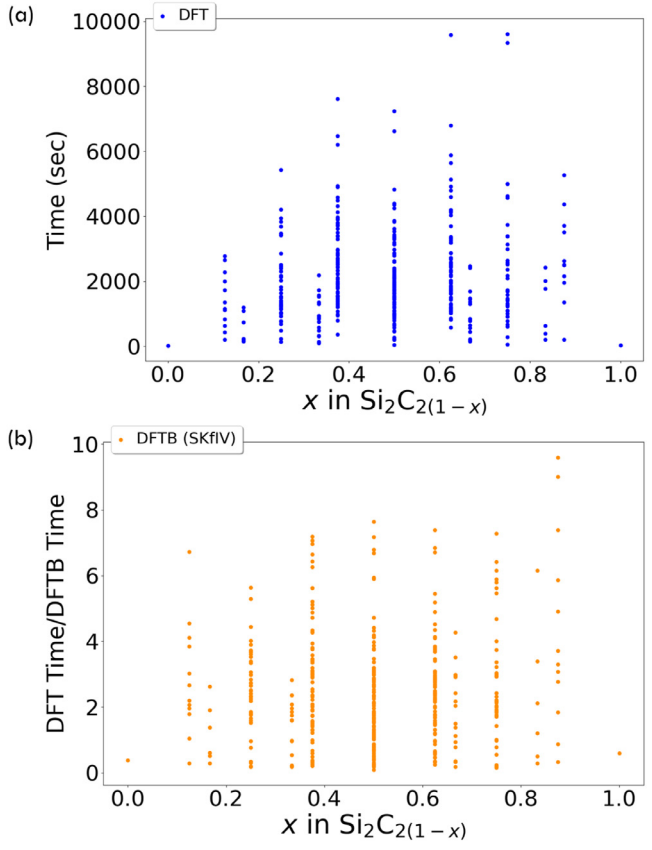

Fig. 8. Comparison of wall times for geometry optimization of various $Si_2C_{2(1-x)}$ compositions calculated via DFT and DFTB. Panel (a) shows the wall time for optimizing each configuration using DFT. Panel (b) shows the ratio between the DFT and DFTB wall times for a geometry optimization of each configuration. Each point corresponds to a different crystal structure.

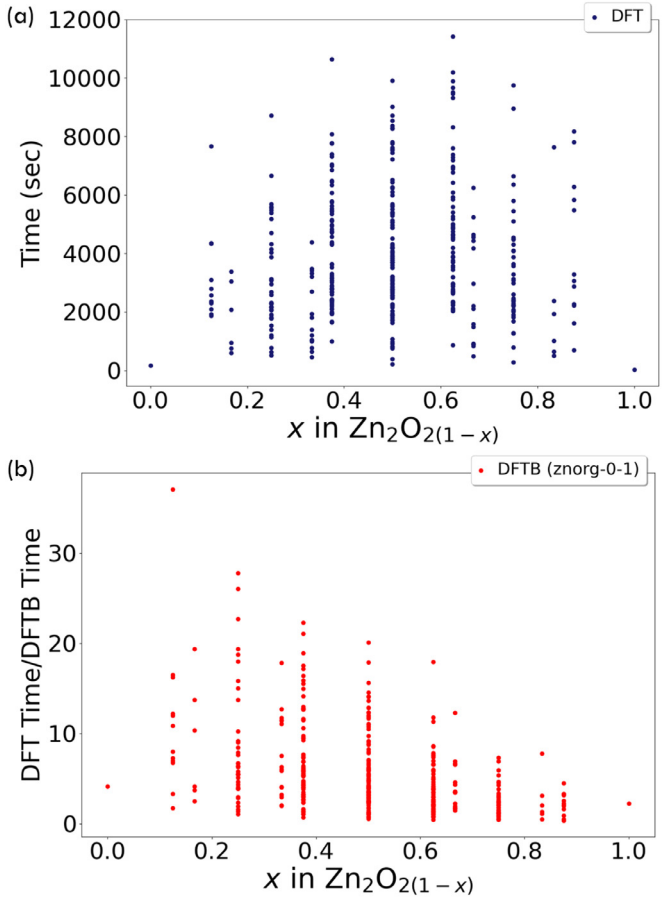

Fig. 9. Comparison of wall times for geometry optimization of various $Zn_2O_{2(1-x)}$ compositions calculated via DFT and DFTB. Panel (a) shows the wall time for optimizing each configuration using DFT. Panel (b) shows the ratio between the DFT and DFTB wall times for a geometry optimization of each configuration. Each point corresponds to a different crystal structure.

Acknowledgment

This work was supported by the U.S. Department of Energy, National Energy Technology Laboratory (NETL), under Award No. DE-FE0030582.

Supplementary material

Supplementary material associated with this article can be found in the online version at 10.1016/j.jmst.2022.10.002

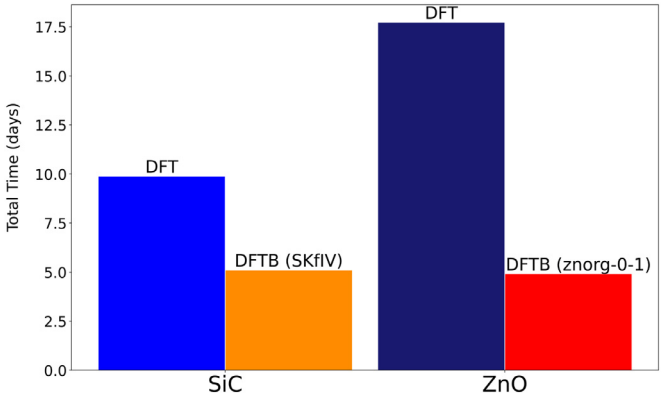

Fig. 10. Comparison of DFT and DFTB total wall times for geometry optimization of all SiC and ZnO configurations. The DFTB calculations used the SKfIV and znorg-0-1 SK files for SiC and ZnO, respectively.

References

[1] C. Freysoldt, B. Grabowski, T. Hickel, J. Neugebauer, G. Kresse, A. Janotti, C.G. Van de Walle, Rev. Mod. Phys. 86 (1) (2014) 253.
[2] M. Ai, J.-W. Zhang, Y.-W. Wu, L. Pan, C. Shi, J.-J. Zou, Chem. Asian J. 15 (22) (2020) 3599–3619.
[3] C.G. Van de Walle, A. Janotti, physica status solidi (b) 248 (1) (2011) 19–27.
[4] R.M. Nieminen, Modell. Simul. Mater. Sci. Eng. 17 (8) (2009) 084001.
[5] P. Hohenberg, W. Kohn, Phys. Rev. B 136 (1964) 864–871.
[6] W. Kohn, L.J. Sham, Phys. Rev. A 140 (1965) 1133–1138.
[7] T. Frauenheim, F. Weich, T. Köhler, S. Uhlmann, D. Porezag, G. Seifert, Phys. Rev. B 52 (1995) 11492–11501.
[8] D. Porezag, T. Frauenheim, T. Köhler, G. Seifert, R. Kaschner, Phys. Rev. B 51 (1995) 12947–12957.
[9] J. Widany, T. Frauenheim, T. Köhler, M. Sternberg, D. Porezag, G. Jungnickel, G. Seifert, Phys. Rev. B 53 (1996) 4443–4452.
[10] S.S. Yamijala, M.B. Oviedo, B.M. Wong, Density Functional Tight Binding Calculations for Probing Electronic-Excited States of Large Systems, John Wiley & Sons, Ltd, 2022, pp. 45–79.
[11] N.V. Ilawe, M.B. Oviedo, B.M. Wong, J. Chem. Theory Comput. 13 (8) (2017) 3442–3454.
[12] N.V. Ilawe, M.B. Oviedo, B.M. Wong, J. Mater. Chem. C 6 (22) (2018) 5857–5864.
[13] M.B. Oviedo, B.M. Wong, J. Chem. Theory Comput. 12 (4) (2016) 1862–1871.
[14] S.I. Allec, Y. Sun, J. Sun, C.-e.A. Chang, B.M. Wong, J. Chem. Theory Comput. 15 (5) (2019) 2807–2815.
[15] S.M. Islam, P.-N. Roy, J. Chem. Theory Comput. 8 (7) (2012) 2412–2423.
[16] K. Leong, M.E. Foster, B.M. Wong, E.D. Spoerke, D. Van Gough, J.C. Deaton, M.D. Allendorf, J. Mater. Chem. A 2 (2014) 3389–3398.
[17] J.M. Rodríguez-Borbón, A. Kalantar, S.S.R.K.C. Yamijala, M.B. Oviedo, W. Najjar, B.M. Wong, J. Chem. Theory Comput. 16 (4) (2020) 2085–2098.
[18] A. Van der Ven, J. Thomas, Q. Xu, J. Bhattacharya, Math. Comput. Simul. 80 (7) (2010) 1393–1410.
[19] A. Van der Ven, J.C. Thomas, Q. Xu, B. Swoboda, D. Morgan, Phys. Rev. B 78 (10) (2008) 104306.
[20] A. Drozdov, M. Eremets, I. Troyan, V. Ksenofontov, S.I. Shylin, Nature 525 (7567) (2015) 73–76.
[21] T. Ishikawa, T. Miyake, K. Shimizu, Phys. Rev. B 100 (17) (2019) 174506.
[22] B. Guigue, A. Marizy, P. Loubeyre, Phys. Rev. B 95 (2) (2017) 020104.
[23] M. Somayazulu, M. Ahart, A.K. Mishra, Z.M. Geballe, M. Baldini, Y. Meng, V.V. Struzhkin, R.J. Hemley, Phys. Rev. Lett. 122 (2) (2019) 027001.
[24] A.P. Drozdov, P.P. Kong, V.S. Minkov, S.P. Besedin, M.A. Kuzovnikov, S. Mozaffari, L. Balicas, F.F. Balakirev, D.E. Graf, V.B. Prakapenka, E. Greenberg, D.A. Knyazev, M. Tkacz, M.I. Eremets, Nature 569 (2019) 528–531.
[25] C.R. Weinberger, X.-X. Yu, H. Yu, G.B. Thompson, Comput. Mater. Sci 138 (2017) 333–345.
[26] X.-X. Yu, C.R. Weinberger, G.B. Thompson, Comput. Mater. Sci. 112 (2016) 318–326.
[27] A.R. Oganov, C.W. Glass, J. Chem. Phys. 124 (24) (2006) 244704.
[28] A.R. Oganov, Y. Ma, A.O. Lyakhov, M. Valle, C. Gatti, Rev. Mineral. Geochem. 71 (1) (2010) 271–298.
[29] Y. Wang, J. Lv, L. Zhu, Y. Ma, Phys. Rev. B 82 (9) (2010) 094116.
[30] Y. Wang, J. Lv, L. Zhu, Y. Ma, Comput. Phys. Commun. 183 (10) (2012) 2063–2070.
[31] D.-H. Yoon, I.E. Reimanis, J. Korean Ceram. Soc. 57 (3) (2020) 246–270.
[32] X. She, A.Q. Huang, O. Lucia, B. Ozpineci, IEEE Trans. Ind. Electron. 64 (10) (2017) 8193–8205.
[33] R. Madar, Nature 430 (2004) 974–975.
[34] J. Casady, R.W. Johnson, Solid State Electron. 39 (10) (1996) 1409–1422.
[35] C. Wöll, Prog. Surf. Sci. 82 (2–3) (2007) 55–120.
[36] M. Elstner, D. Porezag, G. Jungnickel, J. Elsner, M. Haugk, T. Frauenheim, S. Suhai, G. Seifert, Phys. Rev. B 58 (11) (1998) 7260.
[37] A. Santoro, A.D. Mighell, Acta Crystallogr. Section A 28 (3) (1972) 284–287.
[38] A. Santoro, A.D. Mighell, Acta Crystallogr. Section A 29 (2) (1973) 169–175.
[39] G.L.W. Hart, R.W. Forcade, Phys. Rev. B 77 (2008) 224115.
[40] L. Ferreira, S.-H. Wei, A. Zunger, Int. J. Supercomput. Appl. 5 (1) (1991) 34–56.
[41] R. Wyckoff, Crystal Struct. 1 (1963) 85–237.
[42] Y.-N. Xu, W. Ching, Phys. Rev. B 48 (7) (1993) 4335.
[43] S. Desgreniers, Phys. Rev. B 58 (21) (1998) 14102.
[44] G.L. Hart, L.J. Nelson, R.W. Forcade, Comput. Mater. Sci. 59 (2012) 101–107.
[45] B. Puchala, A. Van der Ven, Phys. Rev. B 88 (2013) 094108.
[46] G. Kresse, J. Hafner, Phys. Rev. B 47 (1993) 558–561.
[47] G. Kresse, J. Furthmüller, Phys. Rev. B 54 (1996) 11169–11186.
[48] P.E. Blöchl, Phys. Rev. B 50 (1994) 17953–17979.
[49] G. Kresse, D. Joubert, Phys. Rev. B 59 (1999) 1758–1775.
[50] J.P. Perdew, K. Burke, M. Ernzerhof, Phys. Rev. Lett. 77 (1996) 3865–3868.
[51] S. Liu, E. Martínez, J. LLorca, Acta Mater. 195 (2020) 317–326.
[52] D. Porezag, T. Frauenheim, T. Köhler, G. Seifert, R. Kaschner, Phys. Rev. B 51 (19) (1995) 12947.
[53] G. Seifert, D. Porezag, T. Frauenheim, Int. J. Quantum Chem. 58 (2) (1996) 185–192.
[54] T. Frauenheim, G. Seifert, M. Elsterner, Z. Hajnal, G. Jungnickel, D. Porezag, S. Suhai, R. Scholz, physica status solidi (b) 217 (1) (2000) 41–62.
[55] T. Frauenheim, G. Seifert, M. Elstner, T. Niehaus, C. Köhler, M. Amkreutz, M. Sternberg, Z. Hajnal, A. Di Carlo, S. Suhai, J. Phys. Condens. Matter 14 (11) (2002) 3015.
[56] A.F. Oliveira, G. Seifert, T. Heine, H.A. Duarte, J. Braz. Chem. Soc. 20 (7) (2009) 1193–1205.
[57] G. Seifert, J.-O. Joswig, Wiley Interdiscip. Rev. Comput.Mol. Sci. 2 (3) (2012) 456–465.
[58] M. Gaus, Q. Cui, M. Elstner, J. Chem. Theory Comput. 7 (4) (2011) 931–948.
[59] M. Bezi Javan, Appl. Phys. A 113 (1) (2013) 105–113.
[60] R. Khalil, F. Hussain, N.A. Niaz, J. Mater. Phys. Sci. 2 (2) (2021) 88–94.
[61] O. Arayawut, T. Kerdcharoen, C. Wongchoosuk, Nanomaterials 12 (11) (2022) 1869.
[62] M. Hellström, K. Jorner, M. Bryngelsson, S.E. Huber, J. Kullgren, T. Frauenheim, P. Broqvist, J. Phys. Chem. C 117 (33) (2013) 17004–17015.
[63] V.N. Tuoc, T.D. Huan, N.V. Minh, N.T. Thao, J. Phys. Conf. Ser. 726 (2016) 012022.
[64] A.W. Huran, C. Steigemann, T. Frauenheim, B. Aradi, M.A. Marques, J. Chem. Theory Comput. 14 (6) (2018) 2947–2954.
[65] N.H. Moreira, G. Dolgonos, B. Aradi, A.L. da Rosa, T. Frauenheim, J. Chem. Theory Comput. 5 (3) (2009) 605–614.
[66] V.S. Naumov, A.S. Loginova, A.A. Avdoshin, S.K. Ignatov, A.V. Mayorov, B. Aradi, T. Frauenheim, Int. J. Quantum. Chem. 121 (2) (2021) e26427.
[67] T.A. Niehaus, S.T. Melissen, B. Aradi, S.M.V. Allaei, J. Phys. Condens. Matter 31 (39) (2019) 395901.
[68] S. Wang, Z. Fan, R.S. Koster, C. Fang, M.A. Van Huis, A.O. Yalcin, F.D. Tichelaar, H.W. Zandbergen, T.J. Vlugt, J. Phys. Chem. C 118 (20) (2014) 11050–11061.
[69] M.P. Molepo, D.P. Joubert, Phys. Rev. B 84 (9) (2011) 094110.
[70] P. Erhart, A. Klein, K. Albe, Phys. Rev. B 72 (8) (2005) 085213.
[71] C.G. Van de Walle, Phys. Rev. Lett. 85 (5) (2000) 1012.
[72] E.-C. Lee, Y.-S. Kim, Y.-G. Jin, K.-J. Chang, Phys. Rev. B 64 (8) (2001) 085120.
[73] P. Erhart, K. Albe, Phys. Rev. B 73 (11) (2006) 115207.
[74] T.R. Paudel, W.R. Lambrecht, Phys. Rev. B 77 (20) (2008) 205202.